Scripta Materialia 238 (2024) 115756

Contents lists available at ScienceDirect

Scripta Materialia

journal homepage: www.journals.elsevier.com/scripta-materialia

Effect of Co on spinodal decomposition and magnetic properties in $Fe_{(67-X)}Cr_{31}Co_XSi_2$ (X=9, 14, 19, 24) medium entropy alloys

Zhaolong Xiang [a,b,c], Lin Zhang [a], Bailing An [a,b], Yan Xin [b], Rongmei Niu [b], Jun Lu [b], Robert E. Goddard [b], Tao Wang [a], Engang Wang [a,*], Ke Han [b,*]

[a] Key Laboratory of Electromagnetic Processing of Materials (Ministry of Education), Northeastern University, Shenyang 110819, China
[b] National High Magnetic Field Laboratory, Florida State University, Tallahassee 32310, FL, USA
[c] Shanghai Key Lab of Advanced High-temperature Materials and Precision Forming, Shanghai Jiao Tong University, Shanghai 200240, China

ARTICLE INFO

Keywords:
Medium-entropy alloys
Spinodal decomposition
STEM-HAADF
Magnetic properties

ABSTRACT

We synthesized four $Fe_{(67-X)}Cr_{31}Co_XSi_2$ (X = 9, 14, 19, and 24 at.%) medium-entropy alloys and investigated the effect of Co on the connection between magnetic properties and spinodal structure. When the value of X was increased from 9 to 14 at.%, both the volume fraction of α_1 phase and the composition difference between α_1 and α_2 phases increased, leading to an increase in coercivity. This increase also resulted in an increase in the size of α_1 phase, leading to a decrease in remanence. When the value of X was increased beyond 14 at.%, both coercivity and remanence were significantly enhanced, even though the volume fraction of the α_1 phase remained unchanged. We attribute this enhancement to (1) intensification of the composition fluctuation in the spinodal structure, (2) increase in lattice misfits, and (3) refinement of the α_1 phase. Our results will be valuable in future magnet design.

Because of their excellent magnetic properties, conventional magnetic alloys, such as NdFeB [1–3], SmCo [4,5], and MnGa [6], are currently used in electric motors, wind turbines, and microwave devices. However, their mechanical strength, fracture toughness, and other mechanical properties need to be improved. High-entropy alloys (HEAs) and multi-principal element alloys, originally developed in 2004 by Yeh et al. [7] and Cantor et al. [8], exhibit high fracture toughness [9–12], excellent strength-ductility balance [13–16], good hydrogen embrittlement resistance [17–19], high strength at high temperatures [20,21], and good thermal stability [22–24]. Recently, researchers designed medium-entropy alloys (MEAs) with better mechanical properties than HEAs [25–29]. To improve the mechanical properties of magnetic materials, scientists and engineers have started to investigate the magnetic properties of both HEAs and MEAs.

Rajesh et al. synthesized an HEA ($Al_{20}Fe_{20}Mg_{20}Ni_{20}Ti_{20}$) with the typical properties of soft magnetic materials [30]. This alloy reached a saturation magnetization (M_S) of 54.28 emu/g while maintaining a coercivity (Hc) of 43.4 Oe. In addition to Fe and Ni, Co has the potential to contribute strong magnetic properties to MEAs and HEAs. Chen et al. increased the M_S value of an HEA ($FeCoNiCu_{0.2}Si_{0.2}$) via grain refinement [31]. By inducing spinodal decomposition, Rao et al. generated a ferromagnetic (Fe-Co)-rich phase that led to a significant increase in both the Curie temperature and magnetization in an MEA ($Fe_{15}Co_{15}Ni_{20}Mn_{20}Cu_{30}$) [32].

Liu et al. studied the effects of Co on the magnetic properties of AlNiCo8. The results showed that the coercivity increased with increasing Co [33]. The intrinsic coercivity (Hci) and maximum energy ($(BH)_{max}$) of NdFeB improved significantly after the addition of an appropriate amount of Co [34]. The magnetic properties of FeCrCo also increased with increasing Co. For low-cobalt-content (5–9 wt.%) FeCrCo, $(BH)_{max}$ could reach 2–6 MGOe [35–37]. For medium-cobalt (11–15 wt.%) FeCrCo, $(BH)_{max}$ could attain 5–7 MGOe [38,39]. For high-cobalt (20–25 wt.%) FeCrCo, $(BH)_{max}$ could realize 8 MGOe [40]. In addition, Co-containing magnetic HEAs, such as FeCrCoNiAl [41], CoFeMnNiAl [42], and CoCrFeNiTi [43] have been designed. Although efforts have been devoted to producing high magnetic properties in HEAs and MEAs with various levels of Co content, the effects of Co on the microstructure and composition at the ultrafine scale have not yet been investigated. The aim of this study is to assist future investigations by assembling a set of parameters based on atomic-scale measurements of the microstructures and compositions of various Co-containing alloys. Using these parameters, the magnetic properties of MEAs and HEAs can

* Corresponding authors.
E-mail addresses: egwang@mail.neu.edu.cn (E. Wang), han@magnet.fsu.edu (K. Han).

https://doi.org/10.1016/j.scriptamat.2023.115756
Received 10 March 2023; Received in revised form 16 August 2023; Accepted 4 September 2023
Available online 9 September 2023

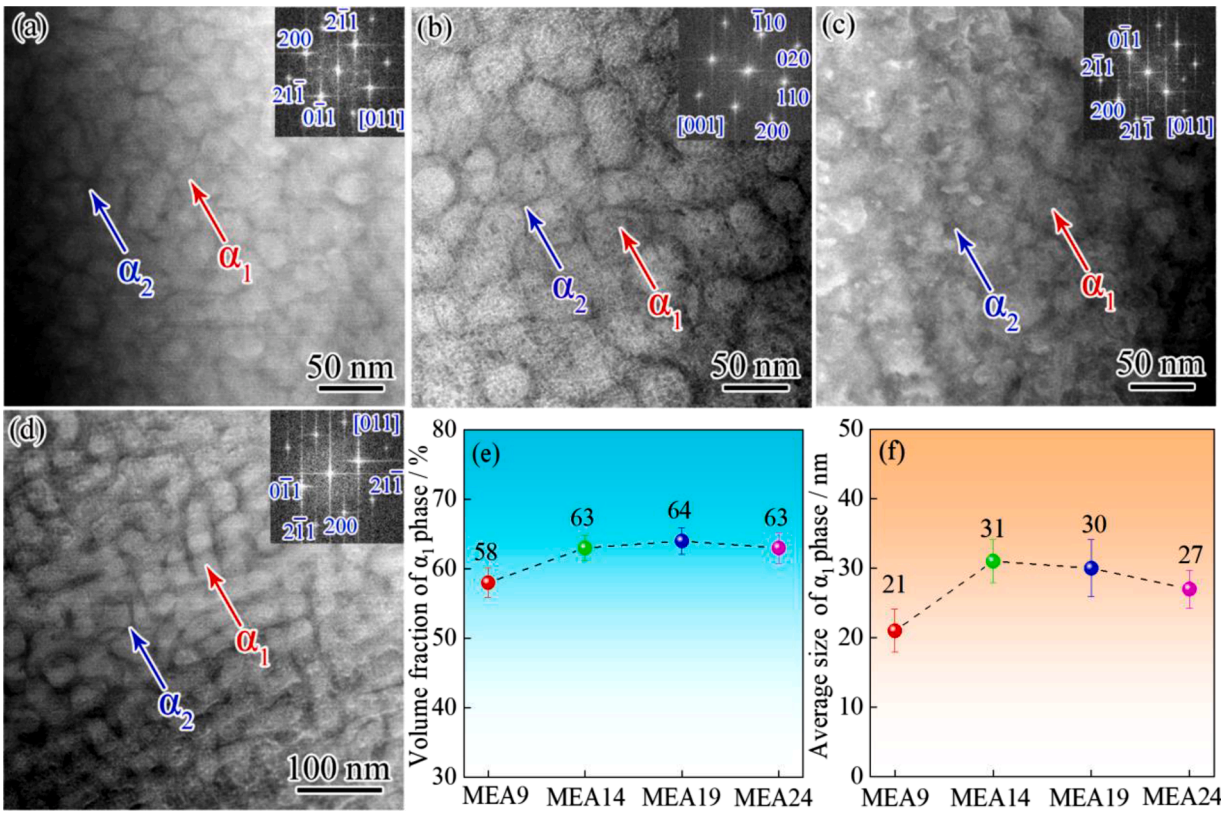

Fig. 1. STEM-HAADF images showing the distribution of the α_1 and α_2 phases with graphic analysis of the volume fraction and the average size of the α_1 phase in samples after step aging. In samples that underwent step aging, many particles of α_1 phase (bright contrast) are distributed throughout the surrounding α_2 matrix (dark contrast). (a) Sample MEA9. (b) Sample MEA14. (c) Sample MEA19. (d) Sample MEA24. The insets are Fast Fourier Transform (FFT) images showing that the zone axis is [011] in MEA9, MEA19, and MEA24; and [001] in MEA14. (e) Volume fraction of the α_1 phase. (f) Average size of the α_1 phase.

be fine-tuned.

We prepared four ingots of non-equiatomic $Fe_{(67-X)}Cr_{31}Co_XSi_2$ (X = 9, 14, 19, and 24 at.%) MEAs in a vacuum electric arc furnace. When X exceeded 24 at.%, undesirable second phase formation occurred, leading to a significant decrease in magnetic properties (Supplementary material Fig. S1). Our research therefore focused on alloys with $X \leq 24$ at.%. The purity of the raw materials was higher than 99.95 wt.%. These four ingots were solution-treated for 2 h at 1300 °C under a high-purity Ar atmosphere. Two samples were cut from each of the solution-treated ingots. One sample from each of the solution-treated ingots was used to test the magnetic properties. Subsequently, all other samples were placed in a low-temperature resistance furnace under a high-purity Ar atmosphere for step aging, i.e., aging at 645 °C for 1 h, 620 °C for 1 h, 600 °C for 2 h, 580 °C for 3 h, 560 °C for 4 h, 540 °C for 5 h, and 520 °C for 6 h and then cooled to room temperature. The step-aged samples are denoted as MEA9, MEA14, MEA19, and MEA24 according to their Co content.

Scanning transmission electron microscopy (STEM) specimens for microstructural examination were prepared by slicing thin sheets from all step-aged samples. The specimens were ground to a thickness of 30 μm. From each, a 3 mm-diameter disk was punched and glued onto a copper ring. The samples were ion-milled first with 5 keV at an incidence angle of 8° and then with 3 keV at 6° incidence angle using a Gatan PIPS. The microstructure was observed using STEM (JEM JEOL-ARM200Cf) equipped with a HAADF-STEM (JEOL) detectors. The elemental compositions of the phases in FeCrCoSi were tested using energy-dispersive spectroscopy (EDS) in STEM. The open-source software, strain++ for geometric phase analysis (GPA) was used to map the coherent strain field from the atomic-resolution STEM-HAADF images [44]. At 298 K, the hysteresis loops of all the solution-treated and step-aged samples were measured using vibrating sample magnetometry (VSM) in a physical property measurement system (PPMS) manufactured by Quantum Design Inc., with a maximum applied field of 9T.

In all samples that underwent step aging, the homogeneous mother α phase decomposed into daughter α_1 and α_2 phases. The resulting microstructure comprised particles of the α_1 phase distributed throughout the surrounding α_2 matrix (Fig. 1). When the Co content was increased from 9 to 14 at.%, the volume fraction of α_1, measured from STEM-HAADF images, increased by 9%. When the Co content was increased above 14 at.%, the volume fraction of α_1 remained practically unchanged (Fig. 1e). The average size of the α_1 phase reached a maximum of 33 nm when the Co content reached 14 at.%. When the Co content was further increased to 19 and 24 at.%, the average size of the α_1 phase decreased by 9% and 18%, respectively, indicating that increasing the Co content beyond 14 at.% refined the microstructure of the alloys (Fig. 1f).

For step-aged samples, EDS mapping results showed that both Fe and Co were rich in the α_1 phase, but Cr was poor. In contrast, both Fe and Co were poor in α_2, but Cr was rich. For Si, however, no difference was observed between the phases (Fig. 2). Using overlays, we measured five EDS maps to analyze the composition of α_1 and α_2 in each sample (Fig. 2 and supplementary material Table S1). Our results showed that increasing the nominal Co content led to an increase in Co and a decrease in Fe in both the α_1 and α_2 phases, accompanied by a decrease in Cr in α_1 and an increase in Cr in α_2. We could not determine whether Si increased or decreased in either α_1 or α_2 when Co was increased.

For the solution-treated samples that were not subjected to step aging, hysteresis loop testing revealed that the remanence (Br) and coercivity (Hcj) values were below 3.7 emu/cm^3 and 25 Oe, respectively (Supplementary material Fig. S2). In the 9 at.% Co sample that had been subjected to both solution treatment and step aging, Br and Hcj were 9.9 emu/cm^3 and 433 Oe, respectively (Fig. 3). When the Co content was

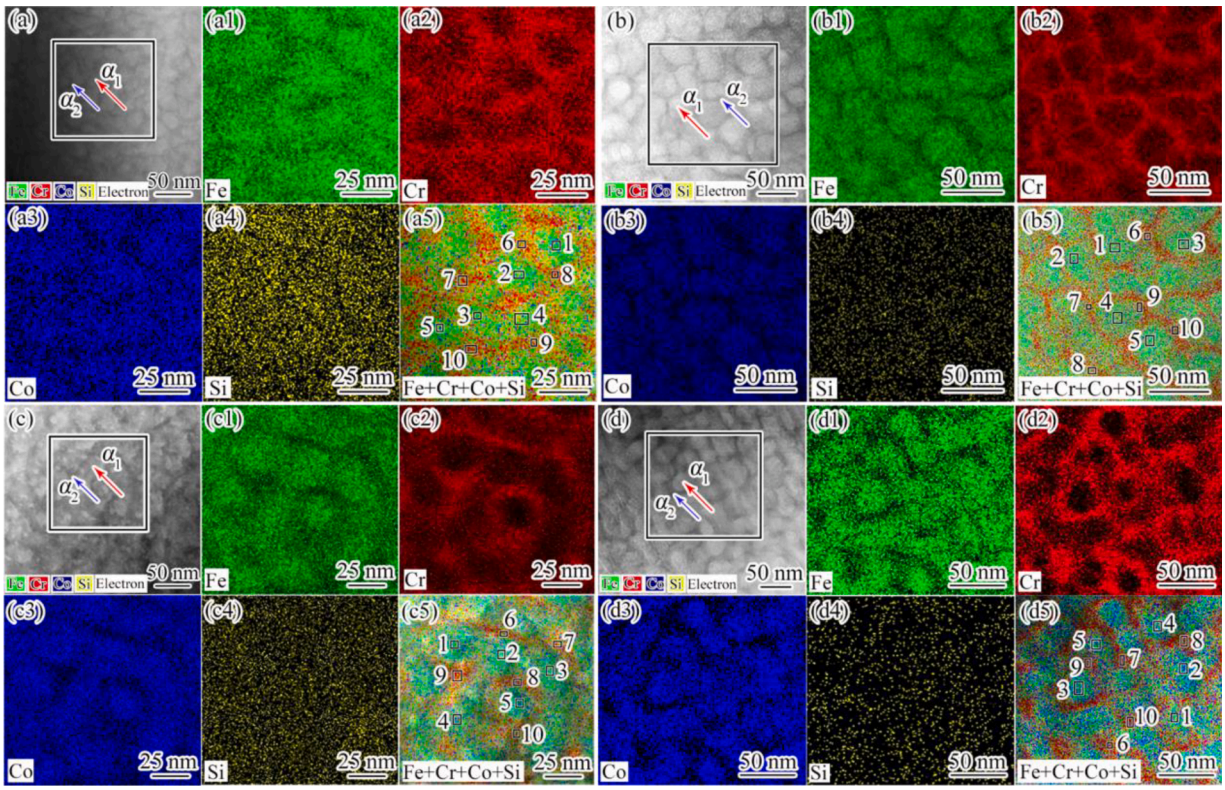

Fig. 2. HAADF/EDS data from samples MEA9, MEA14, MEA19, and MEA24. (a-d) HAADF images of α_1 and α_2 phases in samples MEA9, MEA14, MEA19, and MEA24, respectively. The black squares correspond to the areas of EDS mapping. (a1-d1) EDS maps of Fe. (a2-d2) EDS maps of Cr. (a3-d3) EDS maps of Co. (a4-d4) EDS maps of Si. (a5-d5) Overlay EDS maps of Fe (green), Cr (red), Co (blue) and Si (yellow) in the area delineated in the black squares in Figs. (a-d). (For interpretation of the references to color in this figure legend, the reader is referred to the web version of this article.).

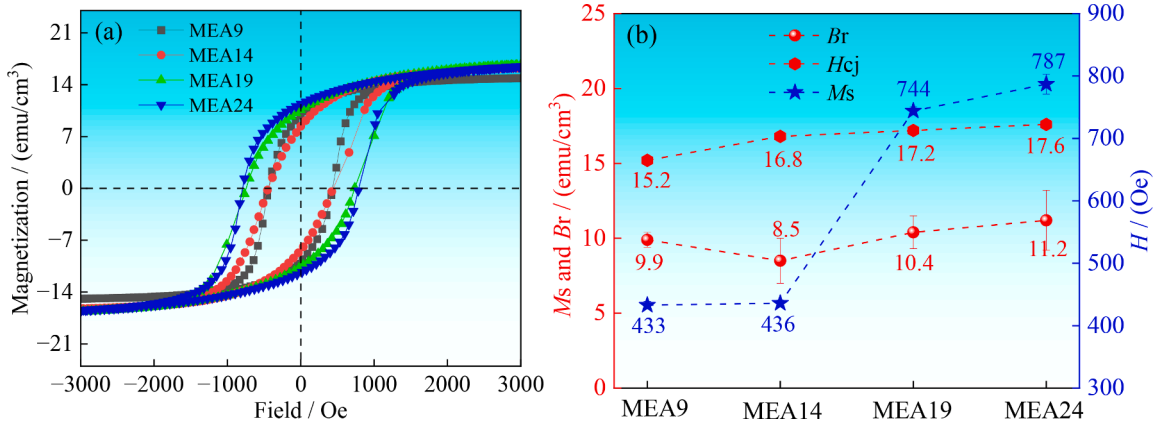

Fig. 3. Magnetic property data for samples MEA9, MEA14, MEA19, and MEA24. (a) Hysteresis loops. (b) Graphs of remanence (*Br*), coercivity (*Hcj*), and saturation magnetization (*Ms*), based on data extracted from the loops in Fig. 3a.

increased to 14 at.%, the sample exhibited a slight increase of 0.7% in *Hcj* accompanied by a 14% decrease in *Br*. When the Co content increased beyond 14 at.%, both *Br* and *Hcj* increased. When the Co content was increased to 24 at.%, both *Br* and *Hcj* reached their maximum values of 11.2 emu/cm^3 and 787 Oe, respectively (Fig. 3). Comparing the properties of the samples before and after step aging indicated that step aging significantly improved both *Hcj* and *Br*.

Measurements of step-aged samples with various levels of Co indicated that changes in magnetic properties are related to: (1) volume fraction, composition, and relative size of the α_1 and α_2 phases, and (2) the overall composition difference between the α_1 and α_2 phases.

In magnetic dual-phase $Fe_{(67-X)}Cr_{31}Co_XSi_2$ alloys, magnetic properties are proportional to the volume fraction of the harder of the two ferromagnetic phases. We used first-principles calculations to arrive at the magnetic moments for the α_1 and α_2 phases of an MEA containing 56.4Fe29Cr14Co0.6Mo (Supplementary material Fig. S3). These calculations show that the α_1 phase is significantly harder than the α_2 phase in terms of ferromagnetic properties. Increasing Co content to 14 at.% resulted in an increase in the volume fraction of the α_1 phase and contributed to a corresponding increase in coercivity. Because the Fe and Co are ferromagnetic elements while Cr and Si are non-ferromagnetic, increasing the content of Fe and Co in the α_1 phase can enhance the magnetic properties of FeCrCo alloys. Our EDS results showed that Fe + Co content increased by 7.1% in the α_1 phase when

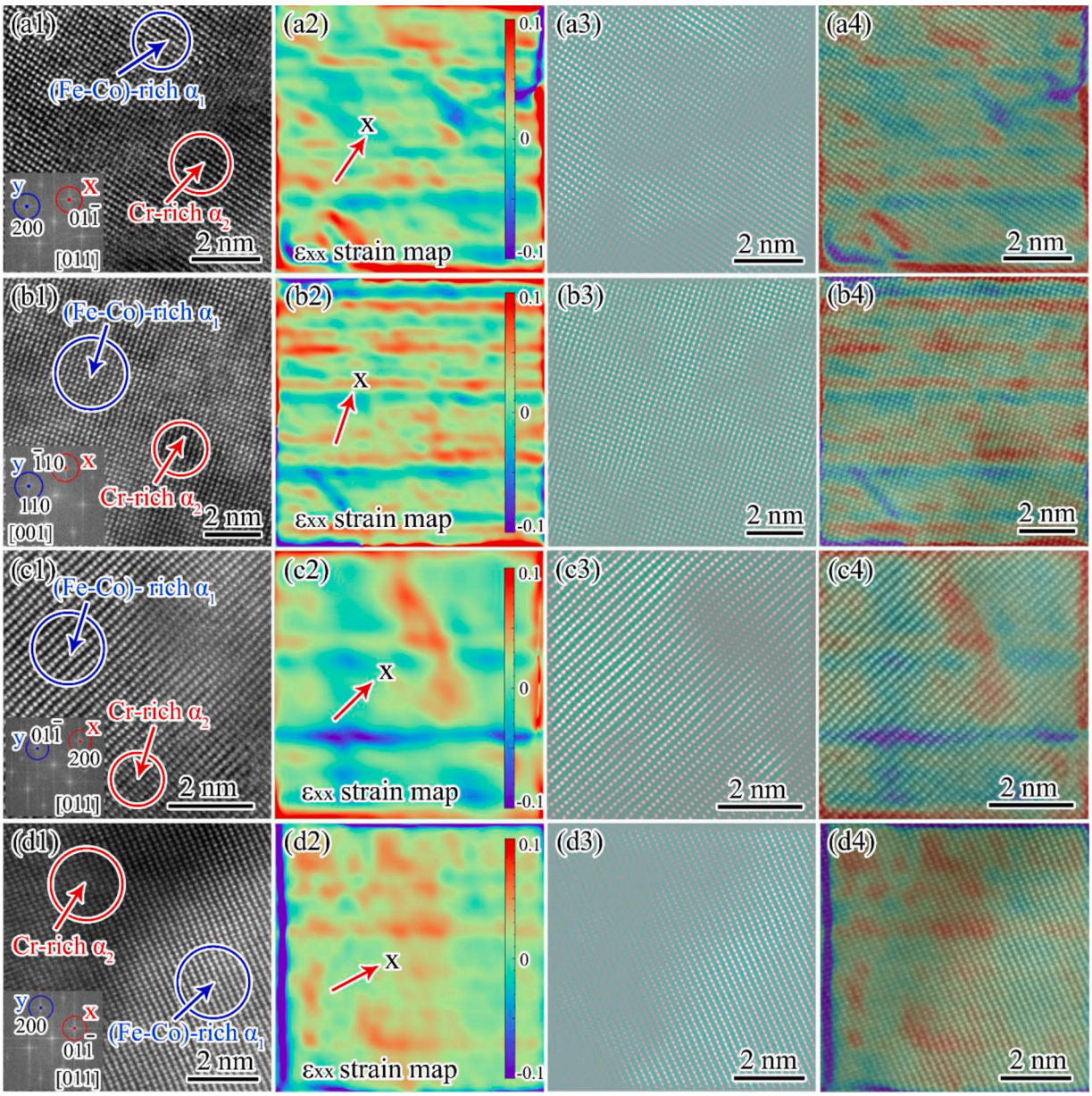

Fig. 4. HAADF images and strain maps showing distribution of coherent strain values between (Fe-Co)-rich α_1 and Cr-rich α_2 phases in samples MEA9, MEA14, MEA19, and MEA24. Figs. (a1 -d1): Atomic-scale STEM-HAADF images of α_1 and α_2 phases in MEA9, MEA14, MEA19, and MEA24, respectively. Figs. (a2-d2): GPA strain maps (ε_{xx}) calculated in the $01\bar{1}$ and 200 directions in figures (a1), (c1), and (d1), and calculated in the $\bar{1}10$ and 110 directions in figure (b1). All the directions are indicated in the insets of FFT images. Figs. (a3-d3): Corresponding inverse FFT images of Figs. (a1-d1). Figs. (a4-d4): The HAADF-STEM images from (a1-d1) overlapped with the ε_{xx} strain maps (a2-d2), respectively. Red regions indicate positive strain and blue regions indicate negative strain. (For interpretation of the references to color in this figure legend, the reader is referred to the web version of this article.).

overall Co content was increased from 9 to 14 at.% (Supplementary material Fig. S4). This increase of ferromagnetic elements in the α_1 phase may also contribute to an increase in coercivity.

Remanence, however, decreased as Co content increased to 14%. Zhou et al. concluded that, in alnico alloys, magnetic properties increased when the α_1/α_2 phase boundary hindered the movement of the domain wall [45]. Their results indicated that a decreased interface area degrades magnetic properties. In our $Fe_{(67-X)}Cr_{31}Co_XSi_2$ alloys, the size of α_1 particles increased as Co increased to 14 at.%, producing fewer α_1/α_2 interfaces (Fig. 1e). This coarsening of α_1 particles could be the prominent reason for the decrease in remanence.

Once the Co content of the samples exceeded 14 at.%, both coercivity and remanence began to increase. Because the volume fraction of the α_1 phase had ceased increasing by that point, it played no role in the subsequent increase of magnetic properties. We therefore attributed this synchronized increase to (1) an increase in the content of Fe + Co in α_1; (2) an increase in the composition difference between the two phases, and (3) a decrease in the size of α_1. For the sample containing 24 at.% Co, both the composition difference and the Fe + Co content reached maximum values, and the size of the α_1 phase reached its minimum, with the result that both coercivity and remanence reached the maximum. Because the smaller wave length resulting from spinodal decomposition enhances magnetic properties in certain cobalt alloys, we believe that the size of the α_1 phase is critical for improving magnetic properties [46–49].

The value of the remanence (*Br)* for spinodal alloys can be estimated as [45]:

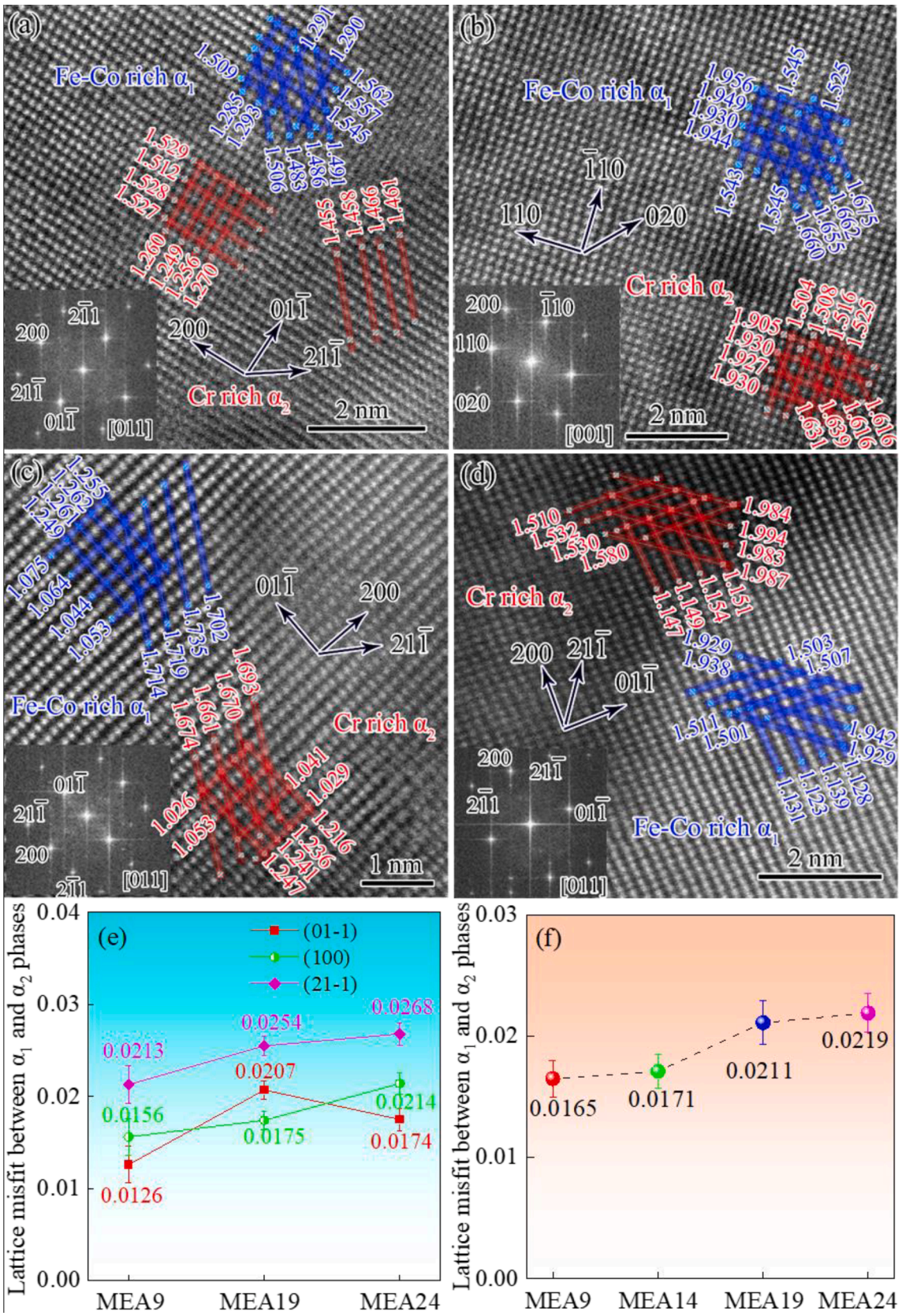

Fig. 5. Analysis of lattice misfit between α_1 and α_2 phases in samples MEA9-MEA24. (a) HAADF-STEM image of MEA9. (b) Image of MEA14. (c) Image of MEA19. (d) Image of MEA24. The insets in (a) - (d) show the corresponding FFT images. All the HAADF images contain both α_1 (bright regions) and α_2 (dark regions). For all samples, lattice spacing in α_1 phase is measured along blue lines and in α_2 phase along red lines. (e) Lattice misfit in [100], [01$\bar{1}$], and [21$\bar{1}$] in samples MEA9, MEA19, and MEA24. (f) Average lattice misfit in samples MEA9, MEA14, MEA19, and MEA24. The lattice misfit (η) was calculated using the equation $\eta = 2(a_1 - a_2)/(a_1 + a_2)$, where a_1 and a_2 are the lattice constants of the α_1 and α_2 phases [43].

$$B_r = PC^{Fe+Co}M_S \quad (1)$$

where P is the volume fraction of the α_1 phase, C^{Fe+Co} is the concentration of (Fe + Co) in the α_1 phase, M_S is the saturation magnetization of the alloy. Eq. (1) indicates that the magnetization of the α_2 phase can be ignored, provided that the α_2 phase exhibits weak ferromagnetic or even paramagnetic characteristics. When the Co content was increased to 14 at.%, the volume fraction P of the α_1 phase stopped increasing. In other words, because P remains constant while Br continues to increase, remanence is determined not so much by the value for P as by the values for C^{Fe+Co} and M_S. Our data indicated that the concentration of Fe and Co in the α_1 phase and the saturation magnetization of the alloys were gradually increased as the Co content increased from 14 to 24 at.% (Fig. 3 and supplementary material Table S1). This resulted in a corresponding increase in the remanence.

The coercivity (H_{cj}) of FeCrCo alloys can be calculated as follows [50]:

$$H_{cj} = p(1-p)(N_b - N_a)\frac{(M_{s\alpha1} - M_{s\alpha2})^2}{\mu_0 M_s} \quad (2)$$

where $M_{s\alpha1}$ and $M_{s\alpha2}$ are the saturation magnetizations of α_1 and α_2 phases, respectively, N_a and N_b are the demagnetizing factors of α_1 particles along the a and b axes, respectively, M_s the saturation magnetization of the alloy, and μ_0 the permeability of vacuum. The HAADF results showed that the shapes of the α_1 phases in all samples are spherical, indicating that the value for N_b–N_a is the same (Fig. 1). When the concentration of Co increased from 14 to 24 at.%, the volume of the α_1 phase remained unchanged, and the value for M_s increased, implying that the H_{cj} value was determined by the $(M_{s\alpha1} - M_{s\alpha2})^2$ value. As Fe and Co are ferromagnetic and Cr is antiferromagnetic, the Ms value is larger for α_1 than for α_2. The STEM-EDS results showed that, from sample MEA9 to sample MEA24, differences between the α_1 and α_2 phases in their respective levels of Fe, Cr, and Co increased steadily (Supplementary material Fig. S4). These differences reflect an increase in the $(M_{s\alpha1} - M_{s\alpha2})$ value, which may be the predominant reason for higher coercivity in samples with higher Co content. The above results show that the key factor in determining magnetic properties is the magnetic moment between α_1 and α_2 phases.

The coherency strain induced by spinodal decomposition can enhance magnetic properties [32]. Several researchers have found that improved magnetic properties in certain alloys are the direct result of strain-induced magnetocrystalline anisotropy [51–54]. Using strain++ software, we analyzed atomic-resolution STEM-HAADF images of our $Fe_{(67-X)}Cr_{31}Co_XSi_2$ (Co content $\leq$ 24 at.%) alloys in order to calculate strain distribution. In all step-aged samples, spinodal decomposition was accompanied by anisotropic coherency strain (Fig. 4). In most cases, strain values occurred in a wave more or less in the ⟨112⟩ direction, the orientation generally found in Fe-C systems [55].

Using the relative lattice spacing method, we quantified the average lattice misfit induced by spinodal decomposition in each of our four step-aged samples (those with Co content $\leq$ 24 at.%) [56,57]. We measured lattice spacing in the [100], [01$\bar{1}$], and [21$\bar{1}$] directions in the α_1 and α_2 phases of MEA9, MEA19, and MEA24 samples (Fig. 5). Using these values, the average lattice misfit between the two phases for each sample was calculated (Fig. 5e). In all three samples, the lattice misfit in the [21$\bar{1}$] direction was larger than that in either of the other two directions, thus indicating internal strain anisotropy. Other nanostructured composites exhibit similar internal strain anisotropies, which produce unique property changes [58,59]. We believe that the internal strain anisotropy, which was induced by spinodal decomposition in our samples, contributed to the corresponding increase in the magnetic properties.

For the MEA14 sample, we followed the same procedure except that we measured the lattice spacing in the [110], [$\bar{1}$10], and [020] directions (Fig. 5b). We subsequently calculated the average lattice misfit for MEA14 and compared the average lattice misfits of all four samples (Fig. 5f). The results showed that the average lattice misfit increased by only 1.1% when the Co content increased from 9 to 14 at.%, thus leading to only a slight increase in coercivity from sample MEA 9 to sample MEA14. In MEA19 and MEA24 samples, whose Co content increased beyond 14 at.%, lattice misfit increased markedly, leading to sharp increase in magnetocrystalline anisotropy, which consequently produced a significant increase in both coercivity and remanence.

In summary, we studied the correlation between microstructure (volume fractions, sizes, compositions, and lattice parameters for α_1 and α_2 phases) and the magnetic properties of $Fe_{(67-X)}Cr_{31}Co_XSi_2$ ($X \leq 24$ at.%) MEAs. As we increased Co content from 9 at.% to 14 at.%, we found an increase in coercivity that we attributed to three factors: (1) a greater volume fraction of α_1, i.e., the stronger magnetic phase, (2) a greater difference between the composition of the α_1 and α_2 phases, and (3) an increase in the lattice misfit between the two phases. At the same time, remanence showed a decrease that we attributed to the concurrent size increase in the α_1 phase. Once Co exceeded 14 at.%, both coercivity and remanence increased together. We attributed this joint increase to four factors: (1) an increase in the composition of Fe+Co in the α_1 phase, (2) a corresponding decrease in the size of the α_1 phase, and (3) a greater composition difference between the two phases, and (4) a greater lattice misfit between two phases. The volume fraction of the α_1 phase can be considered irrelevant to this joint increase because it had stopped increasing once Co reached 14 at%.

Declaration of Competing Interest

The authors declare that they have no known competing financial interests or personal relationships that could have appeared to influence the work reported in this paper.

Acknowledgements

This work was supported by the National Natural Science Foundation of China (51674083, No. U1760206), and 111 Project (2.0) of China (BP0719037). A portion of this study was performed at the National High Magnetic Field Laboratory (NHMFL), which is supported by the National Science Foundation (Cooperative Agreement No. DMR-1157490, DMR-1644779, and DMR-2128556), and Florida. We thank Mary Tyler for editing the manuscript. Zhaolong Xiang and Bailing An were supported by the China Scholarship Council (CSC).

Supplementary materials

Supplementary material associated with this article can be found, in the online version, at doi:10.1016/j.scriptamat.2023.115756.

References

[1] K. Löewe, C. Brombacher, M. Katter, O. Gutfleisch, Temperature-dependent Dy diffusion processes in Nd-Fe-B permanent magnets, Acta Mater. 83 (2015) 248–255.
[2] W.B. Cui, H. Sepehri-Amin, Y.K. Takahashi, K. Hono, Hard magnetic properties of spacer-layer-tuned NdFeB/Ta/Fe nanocomposite films, Acta Mater. 84 (2015) 405–412.
[3] O. Gutfleisch, M.A. Willard, E. Brück, C.H. Chen, S.G. Sankar, J.P. Liu, Magnetic materials and devices for the 21st century: stronger, lighter, and more energy efficient, Adv. Mater. 23 (2011) 821–842.
[4] B.Z. Cui, X. Liu, A.H. King, G. Ouyang, C.I. Nlebedim, J. Cui, Overcoming mechanical fragility in Sm-Co permanent magnet materials, Acta Mater. 196 (2020) 528–538.
[5] Q. Wang, L. Zheng, S. An, T. Zhang, C. Jiang, Thermal stability of surface modified Sm_2Co_{17}-type high temperature magnets, J. Magn. Magn. Mater. 331 (2013) 245–249.
[6] D.R. Brown, K. Han, T. Siegrist, T. Besara, R. Niu, Magnetic properties of doped Mn-Ga alloys made by mechanical milling and heat treatment, AIP Adv 6 (2016) 2–8.
[7] J.W. Yeh, S.K. Chen, S.J. Lin, J.Y. Gan, T.S. Chin, T.T. Shun, C.H. Tsau, S.Y. Chang, Nanostructured high-entropy alloys with multiple principal elements: novel alloy design concepts and outcomes, Adv. Eng. Mater. 6 (2004) 299–303.

[8] B. Cantor, I.T.H. Chang, P. Knight, A.J.B. Vincent, Microstructural development in equiatomic multicomponent alloys, Mater. Sci. Eng. A. 375–377 (2004) 213–218.
[9] B. Gludovatz, A. Hohenwarter, D. Catoor, E.H. Chang, E.P. George, R.O. Ritchie, A fracture-resistant high-entropy alloy for cryogenic applications, Science 345 (2014) 1153–1158.
[10] Z. Zhang, H. Sheng, Z. Wang, B. Gludovatz, Z. Zhang, E.P. George, Q. Yu, S.X. Mao, R.O. Ritchie, Dislocation mechanisms and 3D twin architectures generate exceptional strength-ductility-toughness combination in CrCoNi medium-entropy alloy, Nat. Commun. 8 (2017) 1–8.
[11] Z.J. Zhang, M.M. Mao, J. Wang, B. Gludovatz, Z. Zhang, S.X. Mao, E.P. George, Q. Yu, R.O. Ritchie, Nanoscale origins of the damage tolerance of the high-entropy alloy CrMnFeCoNi, Nat. Commun. 6 (2015) 1–6.
[12] B. Gludovatz, A. Hohenwarter, K.V.S. Thurston, H. Bei, Z. Wu, E.P. George, R. O. Ritchie, Exceptional damage-tolerance of a medium-entropy alloy CrCoNi at cryogenic temperatures, Nat. Commun. 7 (2016) 1–8.
[13] F. Yang, L. Wang, Z. Wang, Q. Wu, K. Zhou, X. Lin, W. Huang, Ultra strong and ductile eutectic high entropy alloy fabricated by selective laser melting, J. Mater. Sci. Technol. 106 (2022) 128–132.
[14] K.B. Zhang, Z.Y. Fu, J.Y. Zhang, J. Shi, W.M. Wang, H. Wang, Y.C. Wang, Q. J. Zhang, Annealing on the structure and properties evolution of the CoCrFeNiCuAl high-entropy alloy, J. Alloys Compd. 502 (2010) 295–299.
[15] J.Y. He, H. Wang, H.L. Huang, X.D. Xu, M.W. Chen, Y. Wu, X.J. Liu, T.G. Nieh, K. An, Z.P. Lu, A precipitation-hardened high-entropy alloy with outstanding tensile properties, Acta Mater. 102 (2016) 187–196.
[16] J. Moon, O. Bouaziz, H.S. Kim, Y. Estrin, Twinning engineering of a CoCrFeMnNi high-entropy Alloy, Scr. Mater. 197 (2021), 113808.
[17] Q. Zhang, H. Xu, X.H. Tan, X.L. Hou, S.W. Wu, G.S. Tan, L.Y. Yu, The effects of phase constitution on magnetic and mechanical properties of $FeCoNi(CuAl)_x$(x = 0-1.2) high-entropy alloys, J. Alloys Compd. 693 (2017) 1061–1067.
[18] Y.J. Kwon, J.W. Won, S.H. Park, J.H. Lee, K.R. Lim, Y.S. Na, C.S. Lee, Ultrahigh-strength CoCrFeMnNi high-entropy alloy wire rod with excellent resistance to hydrogen embrittlement, Mater. Sci. Eng. A. 732 (2018) 105–111.
[19] Y. Zhao, D.H. Lee, M.Y. Seok, J.A. Lee, M.P. Phaniraj, J.Y. Suh, H.Y. Ha, J.Y. Kim, U. Ramamurty, J.I. Jang, Resistance of CoCrFeMnNi high-entropy alloy to gaseous hydrogen embrittlement, Scr. Mater. 135 (2017) 54–58.
[20] W.R. Wang, W.L. Wang, J.W. Yeh, Phases, microstructure and mechanical properties of AlxCoCrFeNi high-entropy alloys at elevated temperatures, J. Alloys Compd. 589 (2014) 143–152.
[21] O.N. Senkov, G.B. Wilks, D.B. Miracle, C.P. Chuang, P.K. Liaw, Refractory high-entropy alloys, Intermetallics 18 (2010) 1758–1765.
[22] D.B. Miracle, O.N. Senkov, A critical review of high entropy alloys and related concepts, Acta Mater. 122 (2017) 448–511.
[23] E.P. George, D. Raabe, R.O. Ritchie, High-entropy alloys, Nat. Rev. Mater. 4 (2019) 515–534.
[24] Q.F. He, P.H. Tang, H.A. Chen, S. Lan, J.G. Wang, J.H. Luan, M. Du, Y. Liu, C.T. Liu, C.W. Pao, Y. Yang, Understanding chemical short-range ordering/demixing coupled with lattice distortion in solid solution high entropy alloys, Acta Mater. 216 (2021), 117140.
[25] S.S. Sohn, A. Kwiatkowski da Silva, Y. Ikeda, F. Körmann, W. Lu, W.S. Choi, B. Gault, D. Ponge, J. Neugebauer, D. Raabe, Ultrastrong medium-entropy single-phase alloys designed via severe lattice distortion, Adv. Mater. 31 (2019) 1–8.
[26] T.J. Jang, W.S. Choi, D.W. Kim, G. Choi, H. Jun, A. Ferrari, F. Körmann, P.P. Choi, S.S. Sohn, Shear band-driven precipitate dispersion for ultrastrong ductile medium-entropy alloys, Nat. Commun. 12 (2021) 1–9.
[27] H. Luo, S.S. Sohn, W. Lu, L. Li, X. Li, C.K. Soundararajan, W. Krieger, Z. Li, D. Raabe, A strong and ductile medium-entropy alloy resists hydrogen embrittlement and corrosion, Nat. Commun. 11 (2020) 1–8.
[28] S.S. Sohn, D.G. Kim, Y.H. Jo, A.K. da Silva, W. Lu, A.J. Breen, B. Gault, D. Ponge, High-rate superplasticity in an equiatomic medium-entropy VCoNi alloy enabled through dynamic recrystallization of a duplex microstructure of ordered phases, Acta Mater. 194 (2020) 106–117.
[29] M. Schneider, E.P. George, T.J. Manescau, T. Záležák, J. Hunfeld, A. Dlouhý, G. Eggeler, G. Laplanche, Analysis of strengthening due to grain boundaries and annealing twin boundaries in the CrCoNi medium-entropy alloy, Int. J. Plast. 124 (2020) 155–169.
[30] R.K. Mishra, R.R. Shahi, A novel low-density semi-hard magnetic $Al_{20}Fe_{20}Mg_{20}Ni_{20}Ti_{20}$ high entropy alloy, J. Magn. Magn. Mater. 516 (2020), 167342.
[31] C. Chen, H. Zhang, Y. Fan, W. Zhang, R. Wei, T. Wang, T. Zhang, F. Li, A novel ultrafine-grained high entropy alloy with excellent combination of mechanical and soft magnetic properties, J. Magn. Magn. Mater. 502 (2020), 166513.
[32] Z. Rao, B. Dutta, F. Körmann, W. Lu, X. Zhou, C. Liu, A.K. da Silva, U. Wiedwald, M. Spasova, M. Farle, D. Ponge, B. Gault, J. Neugebauer, D. Raabe, Z. Li, Beyond solid solution high-entropy alloys: tailoring magnetic properties via spinodal decomposition, Adv. Funct. Mater. (2021) 31.
[33] T. Liu, W. Li, M. Zhu, Z. Guo, Y. Li, Effect of Co on the thermal stability and magnetic properties of AlNiCo8 alloys, J. Appl. Phys. 115 (2014) 1–4.
[34] A.K. Pathak, M. Khan, K.A. Gschneidner, R.W. McCallum, L. Zhou, K. Sun, M. J. Kramer, V.K. Pecharsky, Magnetic properties of bulk, and rapidly solidified nanostructured $(Nd_{1-x}Ce_x)_2Fe_{14-y}Co_yB$ ribbons, Acta Mater. 103 (2016) 211–216.
[35] S. Jin, N.V. Gayle, Low-cobalt Cr-Co-Fe magnet alloys obtained by slow cooling under magnetic field, IEEE Trans. Magn. 16 (1980) 526–529.
[36] S. Jin, G.Y. Chin, B.C. Wonsiewicz, A low cobalt ternary Cr-Co-Fe alloy for telephone receiver magnet use, IEEE Trans. Magn. 16 (1980) 139–146.
[37] S. Jin, Deformation-induced anisotropic Cr-Co-Fe permanent magnet alloys, IEEE Trans. Magn. 15 (1979) 1748–1750.
[38] H.M. Sugimoto S, M. Okada, The enhancement of the magnetic properties of Fe-Cr-Co-Mo polycrystalline permanent magnet alloys by cold rolling and annealing, J. Appl. Phys. 63 (1988) 3707–3709.
[39] Z. Ahmad, A. Ul Haq, M. Yan, Z. Iqbal, Evolution of phase, texture, microstructure and magnetic properties of Fe-Cr-Co-Mo-Ti permanent magnets, J. Magn. Magn. Mater. 324 (2012) 2355–2359.
[40] H. Kaneko, M. Homma, M. Okada, S. Nakamura, N. Ikuta, Fe-Cr-Co ductile magnet with (BH)max = 8 MGOe, AIP Conf. Proc. 620 (1976) 620–621.
[41] S. Huang, W. Li, X. Li, S. Schönecker, L. Bergqvist, E. Holmström, L.K. Varga, L. Vitos, Mechanism of magnetic transition in FeCrCoNi-based high entropy alloys, Mater. Des. 103 (2016) 71–74.
[42] T. Zuo, Y. Cheng, P. Chen, Z. Gao, Y. Zhang, P.K. Liaw, Structural and magnetic transitions of CoFeMnNiAl high-entropy alloys caused by composition and annealing, Intermetallics 137 (2021), 107298.
[43] R.K. Mishra, P. Kumari, A.K. Gupta, R.R. Shahi, Design and development of $Co_{35}Cr_5Fe_{20-x}Ni_{20+x}Ti_{20}$ high entropy alloy with excellent magnetic softness, J. Alloys Compd. 889 (2022), 161773.
[44] M.J. Hÿtch, E. Snoeck, R. Kilaas, Quantitative measurement of displacement and strain fields from HREM micrographs, Ultramicroscopy 74 (1998) 131–146.
[45] L. Zhou, M.K. Miller, P. Lu, L. Ke, R. Skomski, H. Dillon, Q. Xing, A. Palasyuk, M. R. McCartney, D.J. Smith, S. Constantinides, R.W. McCallum, I.E. Anderson, V. Antropov, M.J. Kramer, Architecture and magnetism of alnico, Acta Mater. 74 (2014) 224–233.
[46] L. Zhou, W. Guo, J.D. Poplawsky, L. Ke, W. Tang, I.E. Anderson, M.J. Kramer, On spinodal decomposition in alnico - a transmission electron microscopy and atom probe tomography study, Acta Mater. 153 (2018) 15–22.
[47] B.Z. Cui, K. Han, H. Garmestani, J.H. Su, H.J. Schneider-Muntau, J.P. Liu, Enhancement of exchange coupling and hard magnetic properties in nanocomposites by magnetic annealing, Acta Mater. 53 (2005) 4155–4161.
[48] K. Ren, X. Tan, H. Li, H. Xu, K. Han, The effects of the addition of Dy, Nb, and Ga on microstructure and magnetic properties of $Nd_2Fe_{14}B$/α-Fe nanocomposite permanent magnetic alloys, Microsc. Microanal. 23 (2017) 425–430.
[49] B.Z. Cui, K. Han, Y. Zhang, J.P. Liu, H. Garmestani, S. Liu, A. Crystallization, morphology and magnetic properties of melt-spun (Nd, Pr, Dy)$_2$(Fe, Co, Mo)$_{14}$B/α–Fe nanocomposites, IEEE Trans. Magn. 40 (2004) 2867–2870.
[50] S. Drapal, The origin of anisotropy in Fe-Cr-Co alloys, Czech, J. Phys. B 37 (1987) 1174–1182.
[51] Y.X. Jia, Y.Y. Wu, S. Zhao, S. Zuo, K.P. Skokov, O. Gutfleisch, C.B. Jiang, H.B. Xu, L10 rare-earth-free permanent magnets: the effects of twinning versus dislocations in Mn-Al magnets, Phys. Rev. Mater. 4 (2020) 94402.
[52] J. Lyubina, I. Opahle, K.H. Müller, O. Gutfleisch, M. Richter, M. Wolf, L. Schultz, Magnetocrystalline anisotropy in L10 FePt and exchange coupling in FePt/Fe_3Pt nanocomposites, J. Phys. Condens. Matter. 17 (2005) 4157–4170.
[53] M. Yi, H. Zhang, O. Gutfleisch, B.X. Xu, Multiscale examination of strain effects in Nd-Fe-B permanent magnets, Phys. Rev. Appl. 8 (2017) 1–11.
[54] L. Zhang, K. Han, X.R. Zhang, E.G. Wang, J. Lu, R. Goddard, Effect of a high magnetic field on hard magnetic multilayered Fe-Pt alloys, J. Magn. Magn. Mater. 490 (2019), 165533.
[55] K. Han, M.J. Van Genderen, A. Böttger, H.W. Zandbergen, E.J. Mittemeijer, Initial stages of Fe-C martensite decomposition, Philos. Mag. A. 81 (2001) 741–757.
[56] K. Han, H.W. Zandbergen, A. Böttger, E.J. Mittemeijer, Crystallography of tempered iron- nitrogen martensite : the roles of (011) twin boundaries, Philos. Mag. A. 80 (2000) 311–366.
[57] K. Han, A.J. Böttger, H.W. Zandbergen, E.J. Mittemeojer, Microstructural changes during tempering of Fe-N martensite: formation of α″-nitride, Philos. Mag. A. 82 (2002) 715–733.
[58] K. Yu-Zhang, J.D. Embury, K. Han, A. Misra, Transmission electron microscopy investigation of the atomic structure of interfaces in nanoscale Cu-Nb multilayers, Philos. Mag. 88 (2008) 2559–2567.
[59] K. Han, A.C. Lawson, J.T. Wood, J.D. Embury, R.B. Von-Dreele, J.W. Richardson, Internal stresses in cold-deformed Cu-Ag and Cu-Nb wires, Philos. Mag. 84 (2004) 2579–2593.